Variation in morphology of gold nanoparticles synthesized by the spontaneous reduction of aqueous chloroaurate ions by alkylated tyrosine at a liquid–liquid and air–water interface

Anita Swami,[a] Ashavani Kumar,[a] Moneesha D'Costa,[b] Renu Pasricha[a] and Murali Sastry*[a]

[a] Materials Chemistry Division, National Chemical Laboratory, Pune - 411 008, India.
 E-mail: sastry@ems.ncl.res.in
[b] Organic Chemistry (Synthesis) Division, National Chemical Laboratory,
 Pune - 411 008, India

We demonstrate the formation of gold nanocrystals of different morphologies using alkylated tyrosine (AT) as a reducing agent at a liquid–liquid and air–water interface. The reduction of aqueous chloroaurate ions occurs in a single step wherein the AT molecule plays the multifunctional role of a phase transfer, reducing and capping agent. Gold nanoparticles formed at the air–water interface are very thin, flat sheet or ribbon-like nanostructures, which are highly oriented in the (111) direction. On the other hand, reduction of aqueous chloroaurate ions at a liquid–liquid interface by AT molecules present in the organic phase yielded nanoparticles having predominantly spherical morphology but with no specific crystallographic orientation. The difference in morphology of the nanoparticles may be due to the different orientational and translational degrees of freedom of the AT molecules and gold ions at these two interfaces. The AT-capped gold nanoparticles were characterized by UV-vis spectroscopy, transmission electron microscopy (TEM), X-ray diffraction (XRD), and nuclear magnetic resonance spectroscopy (^{1}H NMR), while the LB films of flat gold sheets were also studied by X-ray photoemission spectroscopy (XPS).

Introduction

Nanoparticles are well-known for their unique size-dependent optical and electronic properties[1] with potential application in the field of catalysis,[2] as electron microscopy markers,[3] and in gene therapy.[4] A number of experimental methods have been reported for the synthesis of metal nanoparticles over a range of sizes in both polar[5–12] (e.g. water) and non-polar[13–15] organic solvents. It is being increasingly recognized that properties of nanomaterials such as their optical/electronic[16,17] and catalytic activity[18] depend not only on the size of the particles but also their shape. Therefore, there is considerable current interest in developing synthesis methods to control the morphology of nanoparticles. These methods involve the synthesis of nanoparticles in the presence of templates such as porous alumina,[19,20] polycarbonate membranes,[21] carbon nanotubes,[22,23] aqueous surfactant media[24,25] and by using a seeded growth process.[26]

As far as metal and semiconductor nanoparticles are concerned, most of the experimental methods reported so far are based on the synthesis of predominantly rod-like nanoparticles of silver,[27,28] gold,[24,29,30] CdSe,[31] and tungsten sulfide[32] with a tunable aspect ratio and nanoprisms of silver[16]/gold[33] and CdS.[34] In almost all of these protocols, the morphology of the nanoparticles has been tailored by reducing the metal ions externally in the presence of different water-soluble surfactants. In addition, Xia and co-workers have developed methods for the synthesis of silver nanowires,[35a,b] nanocubes,[35c] and triangular nanoplates[35d] through a soft, self-seeding, polyol process. Further to this they have also established the one-step approach to the large scale synthesis of gold, platinum and palladium nanostructures with hollow interiors[35e–g] by the replacement reaction between silver nanostructures and an aqueous precursor metal ion solution. Very recently, we have demonstrated the multifunctional capability of the molecule 4-hexadecylaniline (4-HDA) in the one-step synthesis of gold nanoparticles in non-polar organic media.[15] This molecule plays the role of a phase transfer agent (enabling transfer of $AuCl_4^-$ ions from water to the non-polar organic solvent), reducing agent and capping molecule for the gold nanoparticles thus formed.[15] While the nanoparticles were predominantly spherical in nature, their size could be controlled by varying the metal ion:4-HDA molar ratio in the biphasic reaction medium.[15] Making use of the built-in anisotropy of the air–water interface, we thereafter showed that Langmuir monolayers of 4-HDA on an aqueous subphase of chloroauric acid resulted in the formation of nano-sheets/-ribbons of gold at the air–water interface, the 4-HDA Langmuir monolayer presenting a truly two-dimensional reducing interface.[36] The next logical step is the rational design of amphiphiles that possess polar reducing functional groups that can thereafter be used in the synthesis of metal nanoparticles by the spontaneous reduction of the corresponding metal ions both at the interface between water and a non-polar organic solvent and at the air–water interface.

Our group[37,38] and others[39] have identified the amino acids aspartic acid,[37] tryptophan[38] and tyrosine[39] that are capable of reducing chloroaurate ions under mild experimental conditions leading to the formation of stable solutions of gold nanoparticles. In this paper, the first step in the rational design strategy is taken and illustrated using the reducing amino acid tyrosine suitably alkylated to render it water-insoluble (see the schematic, inset of Fig. 7 later). Reaction of the alkylated tyrosine (AT) with aqueous chloroaurate ions at the interface between water and an organic solvent bearing the AT molecules both under vigorous stirring conditions leads to electrostatic complexation of $AuCl_4^-$ ions with the protonated amine groups of AT, phase transfer of the gold ions into the organic solvent followed by reduction of the metal ions and formation of highly stable gold nanoparticles [Scheme 1(A)] of
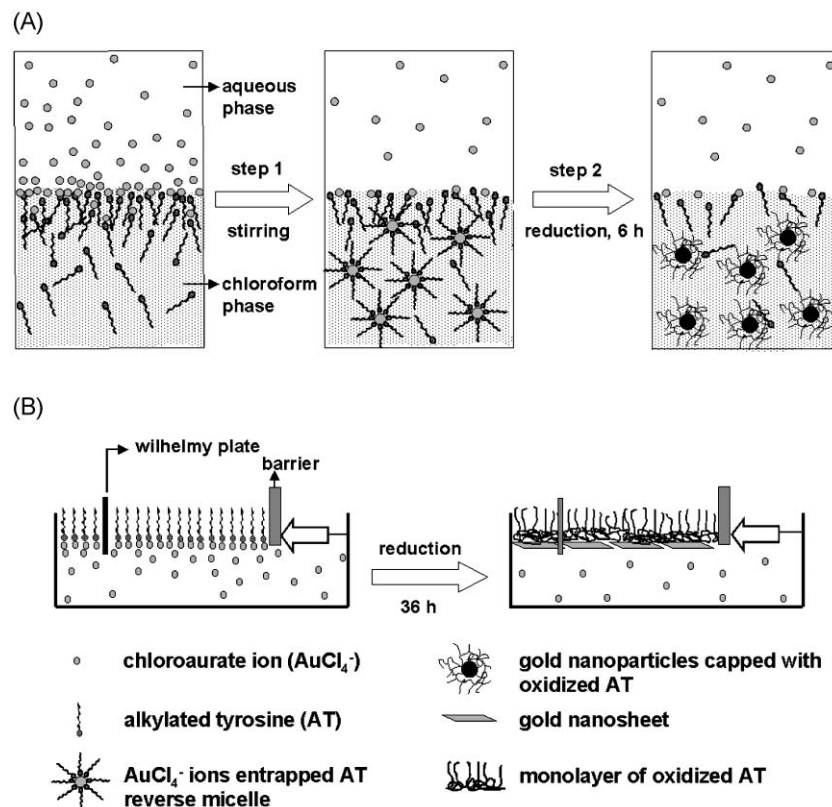
Scheme 1 (A) Diagram showing, step 1: hydrophobization and phase transfer of chloroaurate ions from an aqueous to a chloroform phase by stirring the aqueous chloroauric acid solution with the solution of alkylated tyrosine (AT) in chloroform; step 2: reduction of chloroaurate ions (entrapped in AT reverse micelle) by AT and formation of spherical gold nanoparticles capped and stabilized by oxidized AT. (B) Formation of flat gold nanoribbons/nanosheets at the air–water interface by the spontaneous reduction of chloroaurate ions by the AT Langmuir monolayer (see text for details).

ca. 42 $\pm$ 13 nm diameter. The AT molecules may also be assembled on the surface of aqueous chloroauric acid as the subphase. The reduced orientational and translational degrees of freedom experienced by the AT molecules in the Langmuir monolayer leads to the highly localized reduction of gold ions electrostatically bound to the interface and the formation of nanosheets and nanoribbons [Scheme 1(B)] of highly (111)-oriented gold at the interface. The anisotropic gold nanostructures may be assembled as multilayers by the Langmuir–Blodgett method on suitable substrates. An advantage of this rational design strategy that we hope to exploit in forthcoming studies is the additional degree of freedom to change the size and shape of the reducing headgroup thereby changing the crystallography of the nucleating metal phase at the air–water interface. Presented below are details of the study.

Experimental details

A. Materials

The following chemicals were used as obtained: octadecylamine ($C_{18}H_{39}NH_2$) from Aldrich Chemicals Co.; hydrogen tetrachloroaurate trihydrate (chloroauric acid, $HAuCl_4 \cdot 3H_2O$), chloroform (certified A.R. reagent) and 99% ethanol from S.D. Fine Chemicals Ltd. and L-tyrosine ($C_9H_{11}NO_3$) from Sisco Research Laboratory.

B. Synthesis of alkylated tyrosine (AT)

(a) N-(*tert*-Butyloxycarbonyl)-O-(benzyl)-tyrosinyl octadecylamine. To a stirred clear solution of N-(*tert*-butyloxycarbonyl)-O-(benzyl)-tyrosine (0.20 g, 0.53 mmol) and 1-hydroxybenzotriazole (HOBt) (0.14 g, 1.036 mmol) in anhydrous DMF (5 mL) was added diisopropylcarbodiimide (0.1 mL, 0.64 mmol), followed

by octadecylamine (0.16 g, 0.59 mmol). The solution was stirred at room temperature under a nitrogen atmosphere overnight. TLC indicated formation of the product. The solvent was removed under vacuum and the residue taken up in aqueous sodium bicarbonate (15 mL) and extracted with ethyl acetate (15 mL $\times$ 3). The organic extracts were dried over sodium sulfate and evaporated to obtain 0.49 g crude product, which was purified by column chromatography on silica gel to get 0.28 g pure product (83.5% yield).

^{1}H NMR (CDCl$_3$): δ 7.39 (m, 5H), 7.09 (d, 2H, J = 8.06 Hz), 6.91 (d, 2H, J = 8.06 Hz), 5.63 (br s, 1H), 5.02 (br s, 3H), 4.18 (m, 1H), 3.12 (m, 2H), 2.95 (m, 2H), 1.40 (s, 9H), 1.24 (m, 32H), 0.87 (t, 3H, J = 6.59 Hz).

(b) N-(*tert*-Butyloxycarbonyl)-tyrosinyl octadecylamine. To a solution of N-(*tert*-butyloxycarbonyl)-O-(benzyl)-tyrosinyl octadecylamine (0.09 g, 0.14 mmol) in methanol (5 mL) was added 10% Pd–C (0.01 g, 11% by weight). The reaction mixture was hydrogenated in a Parr hydrogenation apparatus for 4 h at 50 psi. TLC examination indicated completion of the reaction. The catalyst was filtered off and the filtrate was concentrated under vacuum to obtain N-(*tert*-butyloxycarbonyl)-tyrosinyl octadecylamine (0.076 g, 99% yield) as a pure white solid.

^{1}H NMR (CDCl$_3$): δ 7.00 (d, 2H, J = 8.79 Hz), 6.74 (d, 2H, J = 8.79 Hz), 5.83 (m, 1H), 5.13 (m, 1H), 4.21 (m, 1H), 3.14 (m, 2H), 2.94 (m, 1H), 1.41 (s, 9H), 1.30 (m, 2H), 1.24 (s, 30H), 0.86 (t, 3H, J = 6.59 Hz).

(c) Tyrosinyl octadecylamine. The N-(*tert*-butyloxycarbonyl)-tyrosinyl octadecylamine (0.08 g, 0.15 mmol) was dissolved in dry dichloromethane (1 mL). To this, 1 mL of trifluoroacetic acid was added and stirring was continued at room temperature for 20 min, when TLC examination indicated completion of the reaction. The solvents were completely removed by

evaporation under vacuum and co-evaporation with dichloromethane. A gummy product (0.08 g, 97% yield) was obtained which solidified on standing.

^{1}H NMR (CDCl$_3$ + DMSO-d$_6$): δ 6.89 (d, 2H, $J = 8.75$ Hz), 6.62 (d, 2H, $J = 8.34$ Hz), 3.90 (t, 1H, $J = 7.15$ Hz), 2.91–3.04 (m, 2H), 2.90 (d, 2H, $J = 7.15$ Hz), 1.23 (m, 2H), 1.08 (s, 30H), 0.71 (t, 3H, $J = 6.75$ Hz and 7.16 Hz).

C. Synthesis of gold nanoparticles at a liquid–liquid interface

In a typical experiment, 50 mL of a 1×10^{-4} M aqueous solution of HAuCl$_4$ was taken in a beaker along with 50 mL solution of 2×10^{-4} M AT in chloroform. Considering AT as a 2 e$^-$ donor, three equivalents of AT are required for the reduction of two equivalents of AuCl$_4^-$ ions and hence the ratio of AT:Au(III) was maintained at 2:1 where AT molecules are present in excess. The biphasic mixture was stirred vigorously on a magnetic stirrer for 6 h and resulted in a reddish pink color in the organic phase. The chloroform was removed by rotary evaporation, the sample was washed repeatedly with ethanol and the gold nanoparticles obtained as a dry powder. The AT-capped gold nanoparticles could be readily redispersed in chloroform, hexane and toluene and were characterized by different techniques.

### D. Synthesis of gold nanoparticles at the air–water interface

In a typical experiment, 75 µL of AT in chloroform (concentration 1 mg mL^{-1}) was spread on an aqueous 1×10^{-4} M HAuCl$_4$ solution in a Nima model 611 LB trough. A standard Wilhelmy plate was used for surface pressure sensing. Surface pressure–area (π–A) isotherms were recorded at room temperature at compression and expansion rates of 50 cm^2 min^{-1} at different times after spreading of the AT monolayer. After measurement of π–A isotherms, the AT monolayer was compressed to a surface pressure of 20 mN m^{-1} and maintained at this pressure for 36 h. After complete reduction of AuCl$_4^-$ ions, multilayer films of the AT-reduced gold nanoparticles of different thickness were formed by the Langmuir–Blodgett (LB) technique at a surface pressure of 15 mN m^{-1} and a deposition rate of 20 mm min^{-1} with a waiting time of 5 min between dips on carbon-coated transmission electron microscopy (TEM) grids, quartz and Si (111) substrates for TEM, UV-vis spectroscopy, X-ray diffraction (XRD), and X-ray photoemission spectroscopy (XPS) measurements, respectively. The Si (111) and quartz substrates were hydrophobized by depositing three monolayers of lead arachidate prior to transfer of the AT-reduced gold nanoparticle monolayers. The hydrophobization of the support resulted in better transfer ratios of the nanoparticle monolayers. For the LB films grown on different substrates, monolayer transfer was observed both during the upward and downward strokes of the substrate at close to unity transfer ratio.

UV-vis spectroscopy measurements of all the samples were performed on a Hewlett-Packard HP 8542A diode array spectrophotometer operated at a resolution of 2 nm. XRD patterns of the LB films and gold nanoparticles synthesized in chloroform and solution-cast on glass substrates were recorded on a Phillips PW 1830 instrument operating at a voltage of 40 kV and a current of 30 mA with Cu-Kα radiation. TEM measurements on the gold nanoparticle films cast onto carbon-coated TEM grids were carried out on a JEOL instrument model 1200EX at an accelerating voltage of 60 kV. Proton NMR spectra of the solutions of gold nanoparticles synthesized at both liquid–liquid and air–water interfaces were recorded on a Bruker AC 200 MHz instrument and scanned in the range 0–15 ppm. For comparison, the proton NMR spectrum of AT in CDCl$_3$ + DMSO-d$_6$ was also recorded. XPS measurements on the gold nanoparticle LB films were carried

out on a VG MicroTech ESCA 3000 instrument at a pressure of better than 1×10^{-9} Torr. The general scan, C 1s and Au 4f core level spectra were recorded with un-monochromatized Mg-Kα radiation (photon energy = 1253.6 eV) at a pass energy of 50 eV and an electron takeoff angle (the angle between the electron emission direction and the surface plane) of 60°. The overall resolution of measurement is thus ca. 1 eV for the XPS measurements. The core level spectra were background corrected using the Shirley algorithm[40] and the chemically distinct species resolved using a non-linear least squares procedure. The core level binding energies (BEs) were aligned with the adventitious carbon binding energy of 285 eV.

Results and discussion

The inset of Fig. 1A shows a picture of test tubes containing the biphasic mixtures of aqueous HAuCl$_4$ and AT in chloroform before (test tube a) and after the reaction for 6 h under continuous stirring at room temperature (test tube b). The chloroform phase, which is initially colorless takes on a reddish pink hue after reaction indicating formation of gold nanoparticles in the organic phase. Fig. 1A shows the UV-vis spectra recorded from the organic phase as a function of time of reaction of aqueous chloroaurate ions with AT in chloroform. Curves 1, 2, 3 and 4 correspond to the spectra recorded after 0, 2, 4 and 6 h of reaction, respectively. The increase in the surface plasmon resonance centered at ca. 535 nm with time indicates formation of gold nanoparticles in the chloroform phase and that the density of the particles increases steadily during this period of reaction. We would like to mention that after 6 h of reaction, the intensity of the surface plasmon resonance does not increase further, indicating complete reduction of the chloroaurate ions in this time interval. Under stirring conditions, the amine groups in the AT molecules are expected to be fully protonated leading to electrostatic complexation with AuCl$_4^-$ ions at the water–chloroform interface followed by transfer of AuCl$_4^-$ ions from the aqueous to the chloroform phase. We believe that the AuCl$_4^-$ ions become entrapped in the hydrophilic wells of the reverse micelle-like
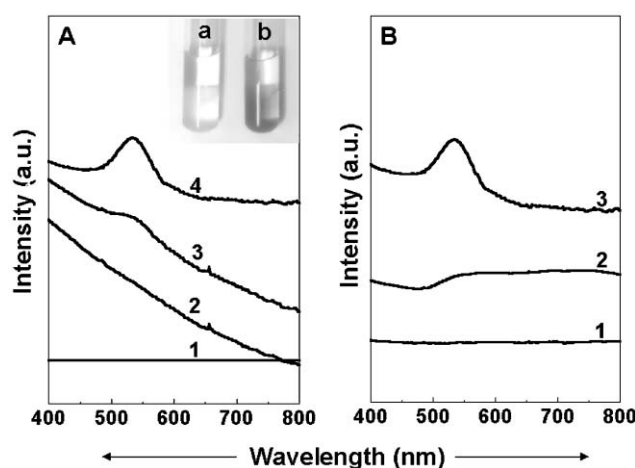
Fig. 1 (A) UV-vis spectra of the chloroform phase recorded as a function of time of reaction of aqueous 1×10^{-4} M HAuCl$_4$ solution with a 2×10^{-4} M chloroform solution of AT. Curves 1, 2, 3 and 4 in the figure correspond to the spectra recorded at time $t = 0$, 2, 4 and 6 h of reaction, respectively. The inset shows a picture of the test tubes containing the biphasic mixtures of AT in chloroform (lower phase) and aqueous HAuCl$_4$ (upper phase) before (test tube a) and after (test tube b) the reaction. (B) UV-vis spectra of 1×10^{-4} M aqueous HAuCl$_4$ solution after reaction with 2×10^{-4} M tyrosine at room temperature (curve 1) and under boiling conditions (curve 2). Curve 3 corresponds to the UV-vis spectrum recorded from the chloroform phase after reaction of AT with aqueous AuCl$_4^-$ ions at a liquid–liquid interface at room temperature (identical to curve 4 in Fig. 1A).

structures formed by the AT molecules, which enables the transfer of gold ions from the aqueous to the organic phase as shown in Scheme 1(A). The gold nanoparticle solutions in chloroform were extremely stable over time, indicating effective capping of the nanoparticles by AT.

It would be instructive to compare the rate of reaction of aqueous gold ions directly with the amino acid tyrosine, which has been implicated in the reduction of gold ions by silk fibroin proteins.[39] Fig. 1B shows the UV-vis spectra recorded from 1×10^{-4} M aqueous chloroauric acid solution after reaction with 2×10^{-4} M tyrosine for 6 h at room temperature (curve 1) and under boiling conditions (curve 2). For comparison, the UV-vis spectrum of gold nanoparticles formed in chloroform by the reaction of aqueous chloroaurate ions with alkylated tyrosine at room temperature as discussed earlier is shown (curve 3). The absence of a clear surface plasmon resonance in the case of the room temperature reduction of gold ions by pure tyrosine (curve 1) indicates that tyrosine does not readily reduce $AuCl_4^-$ ions under these conditions. Boiling the gold ion–tyrosine reaction mixture does lead to the formation of gold nanoparticles in solution (curve 2) but the presence of a broad absorption band indicates considerable aggregation of the gold nanoparticles in solution. A highlight of this part of the work is the finding that after alkylation, tyrosine is capable of rapid and facile reduction of gold ions at room temperature (curve 3). The exact reason for the increase in reducing capability of tyrosine after alkylation is not fully understood. As will be shown below, Langmuir monolayers of AT on aqueous chloroauric acid solution also lead to facile reduction of gold ions and therefore the role of the solvent, chloroform, in enhancing the reduction rate of gold ions by AT may be ruled out. Currently, studies are under way to establish whether alkylation of tyrosine at different sites leads to a variation in its reducing power.

Drop-coated films of AT-capped gold nanoparticles were prepared by solvent evaporation on carbon-coated copper TEM grids and analyzed by transmission electron microscopy (Fig. 2). At low magnification, a number of highly polydisperse gold nanoparticles possessing a variety of shapes are observed (Fig. 2A). The gold nanoparticles assemble into a close-packed
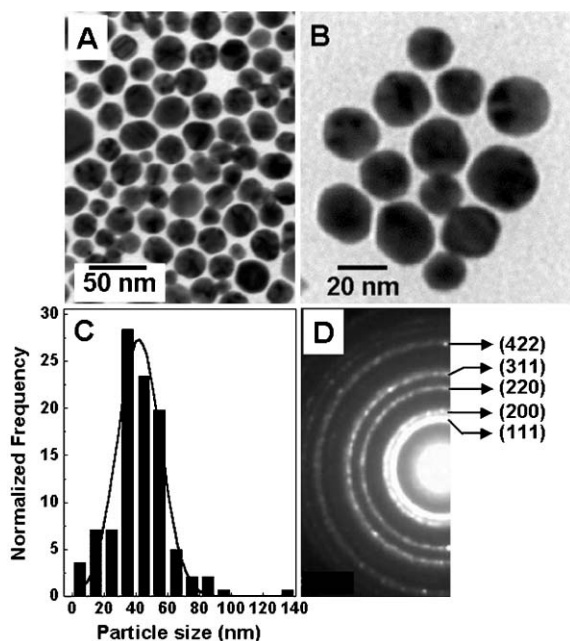
structure, presumably during evaporation of the solvent, chloroform. It is observed from this TEM image that although close-packed, the gold particles are well-separated from each other with an apparently uniform inter-particle separation. This indicates that the gold nanoparticles are capped by an oxidized product of AT that prevents physical contact between the particles and also provides sufficient hydrophobicity to the gold nanoparticles to enable their dispersion in chloroform. At higher magnification, the morphology of the gold nanoparticles is observed more clearly (Fig. 2B). Fig. 2C is a plot showing the particle size distribution (PSD) histogram measured from 150 particles of Fig. 2A and other similar images. The solid line in Fig. 2C is a Gaussian fit to the PSD histogram and this yielded an average particle size of 42 ± 13 nm. Fig. 2D shows the selected area electron diffraction pattern recorded from the gold nanoparticles shown in Fig. 2A. A number of diffuse rings are observed in the electron diffraction pattern and could be indexed based on the fcc structure of gold. The presence of diffuse rings suggests that the gold nanoparticles are polycrystalline.

Fig. 3A shows the XRD pattern recorded from a drop-coated film of AT-stabilized gold nanoparticles synthesized in chloroform on a glass substrate. From the XRD pattern, prominent Bragg reflections at 2θ values of 38.2, 42.2, 66.4 and $79.5°$ are observed which correspond to the (111), (200), (220) and (311) Bragg reflections of fcc gold, respectively, and are thus in agreement with the electron diffraction results discussed above.[41] It is clear from the above measurements that the AT molecule reduces the $AuCl_4^-$ ions at the liquid–liquid interface leading to the formation of stable gold nanoparticles capped by oxidized AT in chloroform.

The above study shows that AT molecules reduce chloroaurate ions spontaneously and lead to the formation of hydrophobized gold nanoparticles of nearly spherical shape dispersible in chloroform. The reducing capability of AT coupled with the in-built anisotropy of the air–water interface provides one with the interesting option of using Langmuir monolayers of AT in the highly localized formation of gold nanoparticles by the spontaneous reduction of chloroaurate ions in the subphase. Fig. 4 shows pressure–area (π–A) isotherms recorded at room temperature and at a compression and expansion rate of 50 cm² min⁻¹ at time intervals of 0, 2, 6, 10 and 20 h after spreading the AT monolayer on the 1×10^{-4} M aqueous $HAuCl_4$ solution as the subphase. The subphase is at a pH of 3.7 and would thus lead to protonation of the amine groups in the AT Langmuir monolayer. This would result in electrostatic complexation of $AuCl_4^-$ ions with the cationic
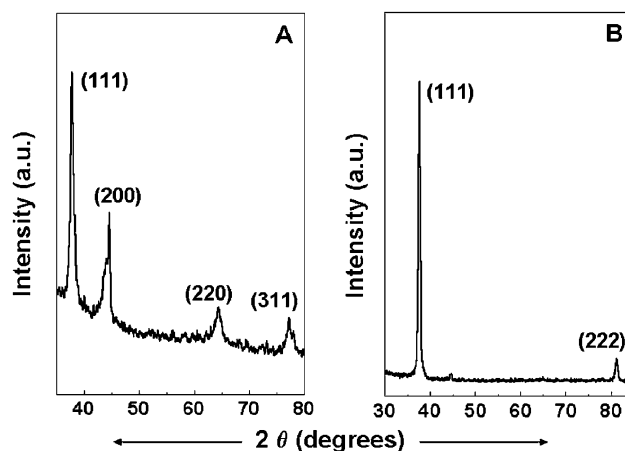
Fig. 2 (A,B) Representative TEM pictures of AT-reduced gold nanoparticles synthesized in chloroform (see text for details). (C) Particle size distribution histogram of more than 150 particles shown in images similar to Fig. 2A. (D) Selected area electron diffraction pattern recorded from the gold nanoparticles shown in Fig. 2A.

Fig. 3 (A) XRD pattern recorded from a drop-coated film of AT-reduced gold nanoparticles in chloroform (see text for details). (B) XRD pattern recorded from a 24 monolayer (ML) LB film of AT-reduced gold nanoparticles at the air–water interface deposited on a glass substrate.
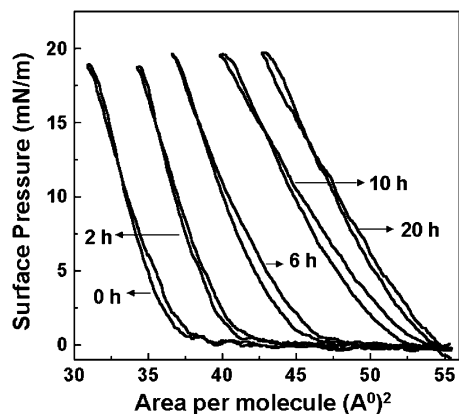
Fig. 4 π–A Isotherms recorded during one compression and expansion cycle of the AT Langmuir monolayer on the surface of the aqueous HAuCl$_4$ subphase as a function of time of spreading of the monolayer. The times at which the isotherms were recorded are indicated next to the respective curves.

Langmuir monolayer in a manner similar to that occurring at the liquid–liquid interface. A large expansion of the monolayer is observed during the compression from *ca.* 37 Å^2 molecule^{-1} at time $t = 0$ h to *ca.* 55 Å^2 molecule^{-1} at $t = 20$ h. The liftoff area after equilibration of the AuCl$_4^-$ ions at the air–water interface (determined to be 55 Å^2 molecule^{-1}) is considerably larger than the liftoff area for the uncomplexed AT molecules (*ca.* 35 Å^2 molecule^{-1}), which indicates complexation of AuCl$_4^-$ ions to the charged AT monolayer. It was observed that the AT monolayer collapsed at a surface pressure close to 23 mN m^{-1} and, consequently, the π–A isotherms with time were recorded to a limiting pressure of 20 mN m^{-1} (Fig. 4). From the π–A isotherm measurements, a region of reasonable incompressibility is seen to occur up to surface pressures of *ca.* 20 mN m^{-1} and, therefore, multilayer films of the AT–Au complex of different thickness were transferred onto hydrophobized quartz, TEM grids and Si (111) substrates for additional analysis at a surface pressure of *ca.* 15 mN m^{-1}.

The nature of the gold nanostructures formed at the air–water interface was studied by recording the TEM images of a monolayer of the AT-complexed particles after complete reduction of chloroaurate ions. Fig. 5A–D shows representative TEM images of 1 ML (monolayer) of the AT–gold nanofilm recorded 36 h after spreading of the AT monolayer on the surface of the 1×10^{-4} M HAuCl$_4$. It is clear from the images that a large concentration of flat gold nanoribbons/nanosheets is obtained at the air–water interface, in contrast to the spherical gold nanoparticles obtained by the reduction of gold ions by AT in chloroform. The dark regions observed in the nanostructures may be due to folding/buckling of the ribbons/sheets during growth or deposition of the LB film. Regions of overlap between nanosheets are also observed to lead to variation in contrast, indirectly suggesting that the nanosheets are extremely thin. We have observed the formation of similar kinds of ribbons/sheets in our previous study in which a hexadecylaniline Langmuir monolayer was used on the subphase of an aqueous solution of chloroauric acid.[36] In case of the air–water interface, reduction of gold ions is localized to a quasi two-dimensional surface since the reducing AT molecules are restricted to the interface owing to their amphiphilicity. This leads to a high degree of anisotropy in the shape of the nanostructures formed [Scheme 1(B)]. In the case of the liquid–liquid interface, initially the AT molecules are concentrated at the interface because of their amphiphilicity. However under vigorous stirring conditions, complexation of AuCl$_4^-$ ions with AT results in hydrophobization and transfer of AuCl$_4^-$ ions from water to the chloroform phase [Scheme 1(A)] and hence further reduction of gold ions (symmetrically
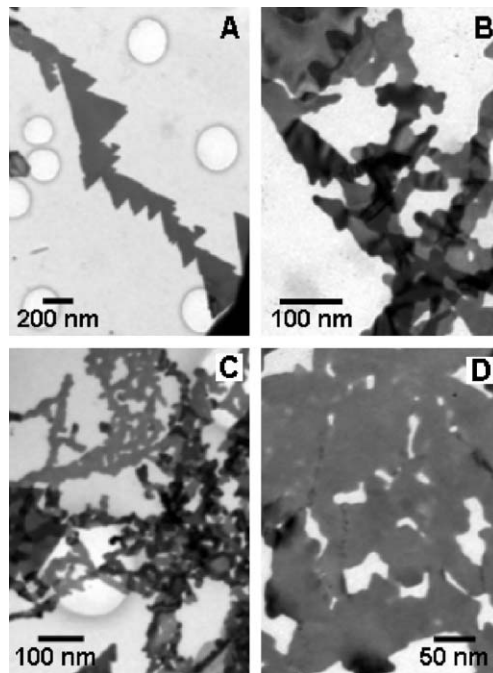
Fig. 5 (A–D) Representative TEM images recorded at different magnifications from one monolayer of AT-reduced gold nanoparticles formed at the air–water interface and transferred onto a carbon-coated TEM grid by vertical lifting.

surrounded by AT molecules) takes place in the chloroform phase and not at the water–chloroform interface. Thus we speculate that the dramatic morphological variation of nanostructures formed at liquid–liquid and air–water interfaces is due to the different degrees of freedom (orientational and translational) experienced by the AT molecules and gold ions at the two interfaces as clearly shown in Scheme 1. The nanoribbons/nanosheets formed at the air–water interface could be transferred by the Langmuir–Blodgett method on glass and quartz substrates for further study by XRD and UV-vis spectroscopy.

Fig. 3B shows the XRD pattern recorded from a 24 ML LB film of the gold nanosheets/nanoribbons transferred onto a glass substrate. This film shows a very strong gold (111) and (222) Bragg reflections at $2\theta = 38.2$ and $81°$, respectively. The peaks corresponding to the (200) and (220) reflections are very weak indicating that the growth is highly face-selective. It is clear from the comparison of Fig. 3A and 3B that highly oriented growth of the gold nanocrystals occurs in the case of gold ions reduced at the air–water interface by the AT Langmuir monolayer. In the case of gold nanoparticle synthesis at a liquid–liquid interface there is no such specific orientation. This result is consistent with the TEM results that show the different morphologies of the gold nanocrystals in the two experiments. In order to check whether formation of highly (111)-oriented, flat gold nanosheets/nanoribbons at the air–water interface is due to epitaxy between the AT Langmuir monolayer and the nucleating gold nanocrystals, efforts were made to break the periodicity of the AT Langmuir monolayer by mixing it with the surfactant, octadecylamine (ODA), in different ratios. π–A Isotherms of mixtures of AT and ODA in the molar ratios 1:1 and 1:3 on an aqueous HAuCl$_4$ subphase did not show any evidence of phase separation and confirms the breakage in periodicity of the AT Langmuir monolayer. The nanogold films formed using these mixed monolayers were transferred onto glass and analyzed by X-ray diffraction. The XRD patterns of these LB films (formed from AT:ODA mixed Langmuir monolayers) also showed very strong (111) Bragg peaks indicating similar face-selective growth in the (111) direction. Thus, this control experiment suggests that the
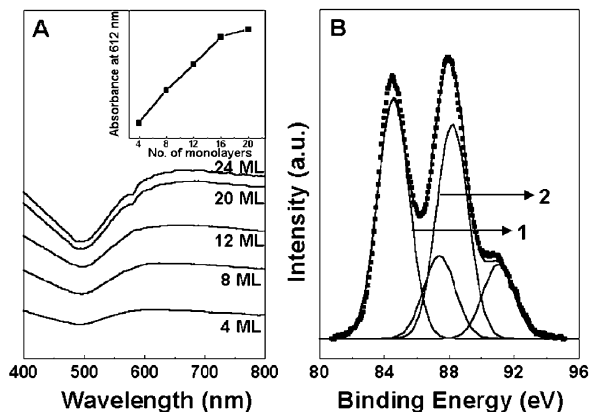
Fig. 6 (A) UV-vis spectra recorded from LB films of AT-reduced gold nanosheets of different thicknesses (number of monolayers indicated next to the respective spectrum) deposited on quartz. The inset is a plot of the intensity of the surface plasmon resonance maximum (absorbance at 612 nm) as a function of the number of monolayers of AT-capped gold nanoparticles in the LB films deposited on quartz. The solid line is an aid to the eye and has no physical significance. (B) Au 4f core level spectrum recorded from a 24 ML AT-reduced gold nanoparticle LB film deposited on a Si (111) substrate and stripped into two chemically distinct spin–orbit components (see text for details).

formation of highly anisotropic, (111)-oriented flat nanostructures at the air–water interface is not the consequence of epitaxy but most probably due to surface energy considerations [the (111) crystallographic face is the most energetically favorable crystal face] and stabilization of the nanosheets/nanoribbons by the oxidized product of AT. The data pertaining to the control experiment have not been shown for brevity.

An important advantage of the synthesis and organization of nanoparticles at the air–water interface is that multilayer superlattice films of close-packed nanoparticle assemblies may be deposited by the LB method. Fig. 6A shows the UV-vis spectra recorded from LB films of the AT–gold nanoribbon complexes of different thicknesses deposited on quartz substrates. A broad absorption band centered at *ca.* 610 nm is observed that increases in intensity with increasing number of monolayers in the LB film. The absorption at 610 nm is due to excitation of surface plasmon vibrations in the gold nanoparticles. This absorption band is red shifted and broadened relative to the narrow absorption band at 534 nm observed for gold nanoparticles synthesized in chloroform. The shift and broadening of the resonance in the LB films indicates considerable aggregation of the particles and is also supported by the TEM results. The inset of Fig. 6A shows the intensity of absorption at 610 nm plotted as a function of the number of monolayers. The monotonic and almost linear increase in the intensity of the absorption band with film thickness indicates that similar amounts of the nanogold–AT monolayers are deposited during each cycle, which may be possibly due to growth of gold multilayers in a lamellar fashion.

A 24 ML AT-capped gold nanoparticle LB film was deposited on a Si (111) substrate and analyzed by XPS. The general scan spectrum showed the presence of strong C 1s, N 1s and Au 4f core levels with no evidence of impurities. The film was sufficiently thick and, therefore, no signal was measured from the substrate (Si 2p core level). The Au 4f core level recorded from the LB film deposited 36 h after spreading the AT monolayer on aqueous chloroauric acid solution is shown in Fig. 6B. The spectrum was background corrected using the Shirley algorithm[40] prior to curve resolution. The Au 4f core level spectrum recorded from the LB film could be stripped into two spin–orbit pairs. The two chemically distinct Au $4f_{7/2}$ components were centered at binding energies (BEs) of 84.5 and 87.5 eV (labelled 1 and 2 in Fig. 6B, respectively). The low

BE component is attributed to electron emission from Au metal[41] while the smaller, high BE component arises from the presence of unreduced Au^{3+} ions in the LB film. The XPS results thus show that a major fraction of the $AuCl_4^-$ ions are reduced to metallic Au by the AT Langmuir monolayer. Based on charge neutrality considerations, it would be expected that one $AuCl_4^-$ ion would bind to one protonated AT molecule. However, since the conversion of Au^{3+} to Au^0 is a $3e^-$ transfer process, it is expected that three equivalents of AT molecules are required for the reduction of two equivalents of gold ions (considering AT as a $2e^-$ donor). Hence all the $AuCl_4^-$ ions bound to the interface would not be fully reduced to Au^0 by the AT Langmuir monolayer, evidence of which is clearly seen by the presence of the fraction of unreduced $AuCl_4^-$ ions in the LB films identified by XPS.

In order to analyse the oxidation product of AT molecules formed consequent to the reduction of $AuCl_4^-$ ions, AT-capped nanoparticles were separated out from the organic solvent and also from the LB films and redispersed in $CDCl_3 + DMSO-d_6$ for ^1H NMR spectroscopic measurements. Curves 1, 2 and 3 in Fig. 7 correspond to the ^1H NMR spectra recorded from pure AT, AT-capped gold nanoparticles formed at the liquid–liquid interface and LB films of AT-reduced gold nanostructures formed at the air–water interface dispersed in $CDCl_3 + DMSO-d_6$, respectively. The NMR spectrum of AT (curve 1) shows a number of prominent resonances that are identified in the schematic given in the inset of the figure. The AT molecule shows chemically shifted protons at 6.8 and 6.6 ppm in curve 1 and are assigned to the two sets of aromatic protons labeled j and i, respectively, in the schematic. The chemically shifted peaks centered at 2.9–3.0 ppm, 1.2, 1.0 and 0.7 ppm correspond to the α-CH_2, β-CH_2, methylene and methyl protons in the C_{18} hydrocarbon chain, respectively. In curves 2 and 3 (AT-reduced gold nanoparticles at the liquid–liquid and air–water interfaces, respectively) there is a complete disappearance of the peaks at 6.8, 6.6, 2.9–3.0 and at 1.2 ppm. Disappearance of signatures of aromatic protons in the ^1H NMR spectra indicate polymerization of AT following the reduction of $AuCl_4^-$ ions. Oxidative oligomerization/polymerization of aromatic diamines in the presence of oxidants such as salts of various transition metals is well-known in the literature.[42] Thus, we believe that the formation of gold nanoparticles at the liquid–liquid and air–water interfaces is accompanied by the polymerization of AT. It is clear from the NMR results that unreacted AT is not present on the gold nanoparticles formed at both the liquid–liquid and
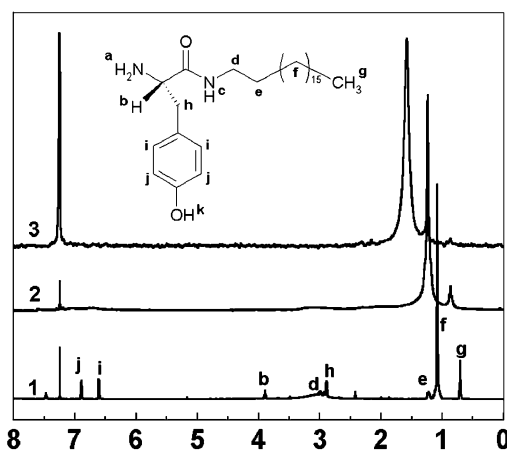
Fig. 7 ^1H NMR spectra recorded from pure AT (curve 1); AT-reduced gold nanoparticles at the liquid–liquid interface synthesized in chloroform and then dispersed in $CDCl_3 + DMSO-d_6$ (curve 2); AT-reduced gold nanoparticle LB film after dissolving in $CDCl_3 + DMSO-d_6$ (curve 3). The inset is a schematic of the AT molecule used in this study identifying the protons that appear in the NMR spectra.

air–water interfaces. At this stage, the extent of polymerization is not comprehensible from ^{1}H NMR studies. This would require separation of the polymer from the nanoparticles for detailed analysis and is currently under study.

In summary, it has been shown that the ability of the amino acid tyrosine to reduce gold ions can be enhanced by alkylation. Alkylation of tyrosine enables the use of this multi-functional molecule in the spontaneous reduction of aqueous gold ions at both the liquid–liquid and air–water interfaces with dramatic differences in the morphology of the gold nanoparticles formed. The rational strategy developed for truly two-dimensional reduction of metal ions at an interface is currently being extended to control the crystallography of the reducing surface and thereby controlling the crystallography of the nucleating nanoparticle face.

Acknowledgements

References

1 C. K. Preston and M. J. Moskovits, *J. Phys. Chem.*, 1993, **97**, 8405.
2 A. J. Hoffman, G. Mills, H. Yee and M. R. Hoffman, *J. Phys. Chem.*, 1992, **96**, 5546.
3 W. Baschong and N. G. Wrigley, *J. Electron Microsc. Tech.*, 1990, **14**, 313.
4 R. Elghanian, J. J. Storhoff, R. C. Mucic, R. L. Letsinger and C. A. Mirkin, *Science*, 1997, **277**, 1078.
5 J. Turkevich, G. Garton and P. C. Stevenson, *J. Colloid Sci.*, 1954, **9**, 26.
6 D. A. Handley, *Colloidal Gold: Principles, Methods and Applications*, M. A. Hayat, ed., Academic Press, San Diego, 1989, vol. 1, ch. 2.
7 D. G. Duff, A. Baiker and P. P. Edwards, *Langmuir*, 1993, **9**, 2301.
8 A. Henglein, *Langmuir*, 1999, **15**, 6738.
9 E. Gachard, H. Remita, J. Khatouri, B. Keita, L. Nadjo and J. Belloni, *New J. Chem.*, 1998, 1257.
10 Y. Mizukoshi, T. Fujimoto, Y. Nagata, R. Oshima and Y. Maeda, *J. Phys. Chem. B*, 2000, **104**, 6028.
11 P. Mukherjee, A. Ahmad, D. Mandal, S. Senapati, S. R. Sainkar, M. I. Khan, R. Ramani, R. Parischa, P. V. Ajayakumar, M. Alam, M. Sastry and R. Kumar, *Angew. Chem., Int. Ed.*, 2001, **40**, 3585.
12 P. Mukherjee, S. Senapati, D. Mandal, A. Ahmad, M. I. Khan, R. Kumar and M. Sastry, *ChemBioChem*, 2002, **3**, 461.
13 M. Brust, M. Walker, D. Bethell, D. J. Schiffrin and R. Whyman, *J. Chem. Soc., Chem. Commun.*, 1994, 801.
14 R. G. Nuzzo and D. L. Allara, *J. Am. Chem. Soc.*, 1993, **105**, 4481.
15 P. R. Selvakannan, S. Mandal, R. Pasricha, S. D. Adyanthaya and M. Sastry, *Chem. Commun.*, 2002, 1334.
16 R. Jin, Y. Cao, C. A. Mirkin, K. L. Kelly, G. C. Schatz and J. G. Zheng, *Science*, 2001, **294**, 1901.
17 T. Huang and R. W. Murray, *J. Phys. Chem. B*, 2001, **105**, 12 498.
18 T. S. Ahmadi, Z. L. Wang, T. C. Green, A. Henglein and M. A. El-Sayed, *Science*, 1996, **272**, 1924.
19 B. R. Martin, D. J. Dermody, B. D. Reiss, M. M. Fang, L. A. Lyon, M. J. Natan and T. E. Mallouk, *Adv. Mater.*, 1999, **11**, 1021.
20 B. M. I. van der Zande, M. R. Bohmer, L. G. Fokkink and C. Schonenberger, *Langmuir*, 2000, **16**, 451.
21 V. M. Cepak and C. R. Martin, *J. Phys. Chem. B*, 1998, **102**, 9985.
22 A. Govindaraj, B. C. Satishkumar, M. Nath and C. N. R. Rao, *Chem. Mater.*, 2000, **12**, 202.
23 S. Fullam, D. Cottell, H. Rensmo and D. Fitzmaurice, *Adv. Mater.*, 2000, **12**, 1430.
24 K. Esumi, K. Matsuhisa and K. Torigoe, *Langmuir*, 1995, **11**, 3285.
25 Y. Y. Yu, S. S. Chang, C. L. Lee and C. R. C. Wang, *J. Phys. Chem.*, 1997, **101**, 6661.
26 N. R. Jana, L. Gearheart and C. J. Murphy, *J. Phys. Chem. B*, 2001, **105**, 4065.
27 S.-W. Chung, G. Markovich and J. R. Heath, *J. Phys. Chem. B*, 1998, **102**, 6685.
28 N. R. Jana, L. Gearhart and C. J. Murphy, *Chem. Commun.*, 2001, 617.
29 K. R. Brown, D. G. Walter and M. J. Natan, *Chem. Mater.*, 2000, **12**, 306.
30 C. J. Johnson, E. Dujardin, S. A. Davis, C. J. Murphy and S. Mann, *J. Mater. Chem.*, 2002, **12**, 1765.
31 X. Peng, L. Manna, W. Yang, J. Wickham, E. Scher, A. Kadanavich and A. P. Alivisatos, *Nature*, 2000, **404**, 59.
32 S. I. Nikitenko, Y. Koltypin, Y. Mastai, M. Koltypin and A. Gedanken, *J. Mater. Chem.*, 2002, **12**, 1450.
33 N. Malikova, I. Pastoriza-Santos, M. Schierhorn, N. A. Kotov and L. M. Liz-Marzan, *Langmuir*, 2002, **18**, 3694.
34 N. Pinna, K. Weiss, J. Urban and M.-P. Pileni, *Adv. Mater.*, 2001, **13**, 261.
35 (*a*) Y. Sun, B. Mayers, T. Herricks and Y. Xia, *Nano Lett.*, 2003, **3**, 955; (*b*) Y. Sun and Y. Xia, *Adv. Mater.*, 2002, **14**, 833; (*c*) Y. Sun and Y. Xia, *Science*, 2002, **298**, 2176; (*d*) Y. Sun and Y. Xia, *Adv. Mater.*, 2003, **15**, 695; (*e*) Y. Sun, B. T. Mayers and Y. Xia, *Nano Lett.*, 2002, **2**, 481; (*f*) Y. Sun, B. Mayers and Y. Xia, *Adv. Mater.*, 2003, **15**, 641; (*g*) Y. Sun and Y. Xia, *J. Am. Chem. Soc.*, 2004, **126**, 3892.
36 A. Swami, A. Kumar, P. R. Selvakannan, S. Mandal, R. Pasricha and M. Sastry, *Chem. Mater.*, 2003, **15**, 17.
37 S. Mandal, P. R. Selvaakannan, S. Phadtare, R. Pasricha and M. Sastry, *Proc. Indian Acad. Sci. (Chem. Sci.)*, 2002, **114**, 513.
38 P. R. Selvakannan, S. Mandal, S. Phadtare, A. Gole, R. Pasricha, S. D. Adyanthaya and M. Sastry, *J. Colloid Interface Sci.*, 2004, **269**, 97.
39 Y. Zhou, W. Chen, H. Itoh, K. Naka, Q. Ni, H. Yamane and Y. Chujo, *Chem. Commun.*, 2001, 2518.
40 D. A. Shirley, *Phys. Rev. B*, 1972, **5**, 4709.
41 D. V. Leff, L. Brandt and J. R. Heath, *Langmuir*, 1996, **12**, 4723.
42 X.-G. Li, M-R. Huang, W. Duan and Y.-L. Yang, *Chem. Rev.*, 2002, **102**, 2925.